Origin of the large magnetoresistance in the candidate chiral superconductor $4H_b$-TaS_2

J. J. Gao,[1,2] J. G. Si,[1,2] X. Luo,[1,*] J. Yan,[1,2] Z. Z. Jiang,[1,2] W. Wang,[1,2] Y. Y. Han,[3] P. Tong,[1] W. H. Song,[1] X. B. Zhu,[1] Q. J. Li,[4] W. J. Lu,[1,†] and Y. P. Sun[3,1,5,‡]

[1]*Key Laboratory of Materials Physics, Institute of Solid State Physics, HFIPS, Chinese Academy of Sciences, Hefei 230031, China*

[2]*Science Island Branch of Graduate School, University of Science and Technology of China, Hefei 230026, China*

[3]*Anhui Province Key Laboratory of Condensed Matter Physics at Extreme Conditions, High Magnetic Field Laboratory, HFIPS, Chinese Academy of Sciences, Hefei, 230031, China*

[4]*State Key Laboratory of Superhard Materials, Jilin University, Changchun 130012, China*

[5]*Collaborative Innovation Center of Microstructures, Nanjing University, Nanjing 210093, China*

(Received 16 May 2020; revised 27 July 2020; accepted 6 August 2020; published 26 August 2020)

The intriguing electronic phase diagram involving charge density wave (CDW) transitions in the TaS_2 system has been widely investigated over the past decade, especially for the $1T$ and $2H$ phases. $4H_b$-TaS_2, regarded as the natural heterostructure that combines the characteristics of $1T$ and $2H$-TaS_2, has also been the focus recently, due to the prospects for fundamental research and device applications. Here, we have systematically investigated the electrical transport properties of $4H_b$-TaS_2 single crystals combined with the band structure calculations and found that the low-temperature phase of candidate chiral superconductor $4H_b$-TaS_2 ($T_c \sim 3.5$ K) at normal state is not the simple CDW but exhibits a strong magnetic field dependence. The most significant result is the emergence of the large magnetoresistance (MR), which may originate from the high mobility of holes and partial compensation. In addition, the symmetry of MR under the low magnetic field has also changed significantly in $4H_b$-TaS_2, which is closely related to the CDW structures formed in the H layers at 22 K. The results are conducive to the understanding of the mechanism of MR appearing in layered CDW compounds, and the presence of MR in $4H_b$-TaS_2 suggests the potential applications for functional devices in the future.

DOI: 10.1103/PhysRevB.102.075138

I. INTRODUCTION

TaS_2 is one of the most studied layered transition-metal dichalcogenides (TMDCs) due to its rich phases and novel properties. The electronic phase diagram involving charge density wave (CDW) transitions in this system can be modified through various methods, suggesting potential applications for functional devices [1–3]. Among the polytypes of TaS_2, $1T$-TaS_2 has been widely investigated for a long time, since it undergoes a series of CDW transitions: From normal metal into the incommensurate CDW (ICCDW) at 550 K, the nearly commensurate CDW (NCCDW) at 350 K, and the commensurate CDW (CCDW) at 180 K, where 12 Ta atoms move slightly towards the central Ta atom and form the superlattice of the $\sqrt{13} \times \sqrt{13}$ so-called David Star. The CDW transitions can be regulated by doping, applying pressure or reducing dimensionality, etc., and even the superconductivity can be induced in $1T$-TaS_2 [4–6]. Due to the theoretical and experimental exploration of the possible quantum spin liquid state, $1T$-TaS_2 has been the focus again recently [7–10], while $2H$-TaS_2 only has a single CDW transition at about 78 K from a conventional metallic phase to the 3×3 ICDW phase [11]. Although the intrinsic superconductivity in $2H$-TaS_2 occurs at a very low temperature, $T_c = 0.8$ K, its transition temperature can be raised to 8.5 K with the external pressure of 10 GPa [12,13]. In addition, the intercalation of $3d$ magnetic elements in $2H$-TaS_2 can generate long-range magnetic order, which has also become an important subject over the past decade [14–16].

Compared with the two phases mentioned above, $4H_b$-TaS_2 has a more intriguing structure and physical properties, which combines the characteristics of $1T$ and $2H$-TaS_2 but is quite different from both [17]. Because of the unique alternating stacked structure, previous reports on $4H_b$-TaS_2 have focused on the characterization of its structure. In particular, spectroscopy measurements, such as the scanning tunneling microscope (STM), etc., have been widely used to determine the properties of different layers and the origin of different CDWs in $4H_b$-TaS_2 [18–21]. However, changes in the electronic structure after the CDW transition and properties of the ground state at low temperature have been ignored. Recently, a report about the chiral superconductivity of $4H_b$-TaS_2 has once again aroused interest in it, which mentions that $4H_b$-TaS_2 is a system that has strong spin fluctuations at normal state [22]. Considering the spin fluctuations, whether the electronic structure would be affected by the magnetic field before the emergence of superconductivity is still a fascinating scientific question. As an effective method, electrical transport measurements under the magnetic field are often used to reflect changes in electronic structure. Actually, R. M. Fleming and R. V. Coleman found the quantum oscillations of

*xluo@issp.ac.cn
†wjlu@issp.ac.cn
‡ypsun@issp.ac.cn

magnetoresistance (MR) and Hall effect in $4H_b$-TaS_2 at low temperatures through electrical transport measurements under the magnetic field as early as 1976 [23,24]. They analyzed the origin of the oscillation and inferred the related electronic structure of $4H_b$-TaS_2. Although the large MR in $4H_b$-TaS_2 was reported, its origin is not sufficiently probed until now.

In this work, we comparatively investigated the features of the band structure, Fermi surface, and the structures of $1T$, $2H$, and $4H_b$-TaS_2 through the first-principles calculations and basic physical measurements. A systematic electrical transport measurement was also performed on $4H_b$-TaS_2, and we found that it exhibits a larger MR than $1T$ and $2H$-TaS_2 at low temperature. The results of further angular MR (AMR) indicate that accompanied by the emergence of larger MR, the symmetry of MR under low magnetic field has changed significantly in $4H_b$-TaS_2, which is closely related to the CDW structures formed in the H layers at 22 K. To find out the origin of large MR in $4H_b$-TaS_2, we also carried out Hall effect measurements. The results suggest that MR in $4H_b$-TaS_2 at low temperature may stem from high mobility of holes and partial compensation.

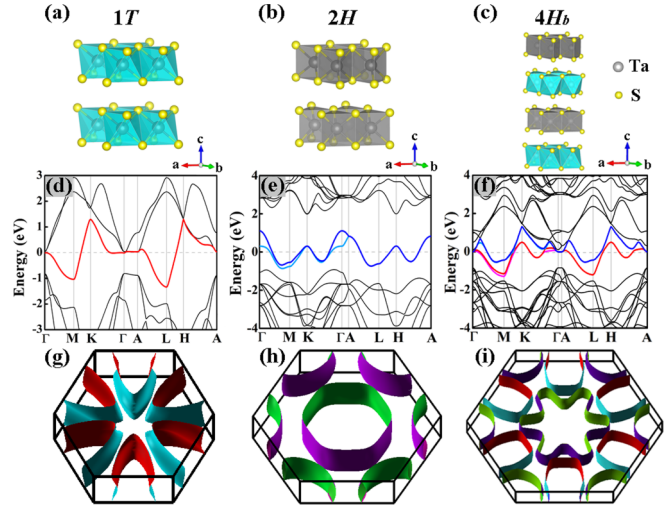

FIG. 1. The crystal structures of (a) $1T$, (b) $2H$, and (c) $4H_b$-TaS_2. The band structures of (d) $1T$, (e) $2H$, and (f) $4H_b$-TaS_2. The colored lines refer to the bands passing through the Fermi surface. Fermi surfaces of (g) $1T$, (h) $2H$, and (i) $4H_b$-TaS_2.

II. EXPERIMENT AND CALCULATION DETAILS

$4H_b$-TaS_2 single crystals were grown by the chemical vapor transport (CVT) method with iodine as the transport agent. Ta and S powders with a mole ratio of 1:2 were weighted and mixed with 0.15 g of I_2, which were placed into silicon quartz tubes. These tubes were sealed under high vacuum and heated for 10 days in a two-zone furnace, where the temperature of source and growth zones were fixed at 780 °C and 680 °C, respectively. Then the quartz tubes were removed from the furnace and quenched in the ice water mixture. Single crystal and powder x-ray diffraction (XRD) experiments were performed by the PANalytical Xpert diffractometer using the Cu Kα1 radiation ($\lambda = 0.15406$ nm) at room temperature. Electrical transport measurements were carried out in a Quantum Design physical property measurement system (PPMS). Magnetic properties were performed by the magnetic property measurement system (MPMS).

The Vienna *ab initio* simulation package (VASP) [25,26] was used to perform structural optimizations and electronic structure calculations. The projector-augmented wave (PAW) [27] method was used, which is parameterized by Perdew-Burke-Ernzerhof (PBE) [28] according to the generalized gradient approximation (GGA). The plane-wave cutoff energy was set to be 450 eV. The convergence criterion for energy was set to be 10^{-6} eV and the structures were fully relaxed until the Hellmann-Feynman force acting on each atom is less than 5×10^{-3} eV/Å. The Fermi surfaces were plotted by using the program XCrySDen [29].

III. RESULTS AND DISCUSSION

TaS_2 has multiple configurations, the most typical of which are the $1T$ type with octahedral structure in the layer and the $2H$ type with trigonal prismatic structure as shown in Figs. 1(a) and 1(b). Another type, called $4H_b$-TaS_2, has an interesting stacked layered structure that includes the characteristics of $1T$ and $2H$. $4H_b$-TaS_2 is composed of alternating layers of $1T$-TaS_2 and $1H$-TaS_2 (half of $2H$-TaS_2), which consists of covalently bound three-atom-thick planar layers of S-Ta-S with the weak van der Waals interaction between the layers, and a unit cell is four layers thick, see in Fig. 1(c). From Figs. 1(d)–1(i), we could find that the features of Fermi surface of the other two polytypes are contained in the Fermi surface of $4H_b$-TaS_2, which is consistent with the previous theoretical reports and even has been demonstrated by experiments [30,31]. However, the differences between them cannot be ignored yet. The Fermi surface of $1T$-TaS_2 seems to be larger than that of $4H_b$-TaS_2, which means that the Fermi surface of $1T$-TaS_2 should shrink to accommodate that of $4H_b$-TaS_2, suggesting charge transfer out of the T layers. With these characteristics, $4H_b$-TaS_2 can be considered as a natural heterostructure, which may exhibit more novel properties.

We have grown single crystals of $1T$, $2H$, and $4H_b$-TaS_2 and performed basic physical measurements on them. Figure 2(a) presents the single crystal XRD patterns recorded $(00l)$ planes of preferred orientation for three polytypes of TaS_2, indicating that the c axis is perpendicular to the plane of the single crystals. The deviations of peak positions suggest the differences of lattice constants among these polytypes. Meanwhile, the powder XRD pattern of $4H_b$-TaS_2 is also collected on crushed single crystals at room temperature. It can be seen in Fig. 2(b) that the powder is single phase without any other secondary phase existing. Structural refinement of powder XRD identifies that all reflections can be indexed with the $P6_3/mmc$ space group. The in-plane resistivity (ρ_{ab}) curve of $4H_b$-TaS_2 can be seen in Fig. 2(c), which shows two CDW transitions, one at 315 K and the other one at 22 K. At the higher transition, the typical $\sqrt{13} \times \sqrt{13}$ CDW structures appear in the octahedral layers, while an incommensurate 3×3 superlattice forms in the trigonal prismatic layers below 22 K, which could be confirmed by STM experiments [20,21]. The superconductivity at a transition temperature $T_c \sim 3.5$ K with a sluggish resistive transition is also observed, T_c of which is four times higher than that of $2H$-TaS_2, as shown in the

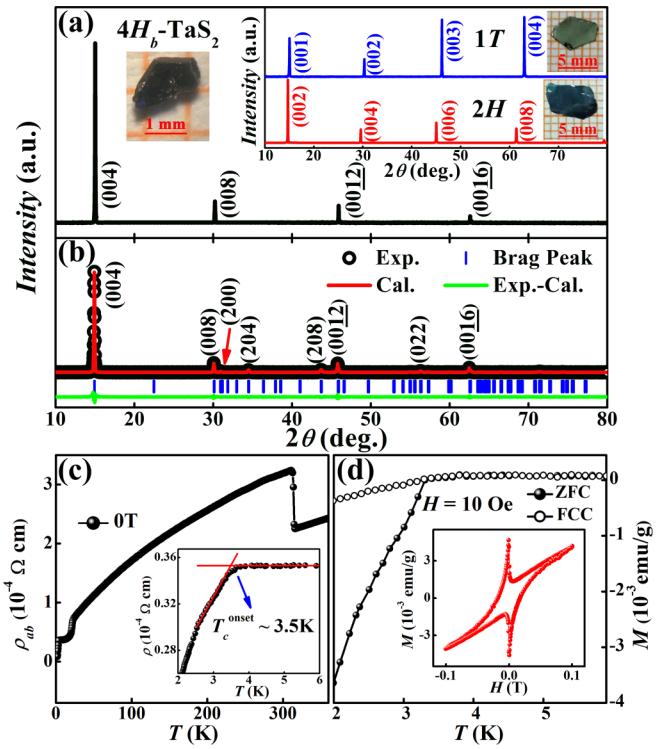

FIG. 2. (a) The single crystal XRD pattern of $4H_b$-TaS_2. The inset (left) presents the picture of the studied crystal, and the right inset shows the single crystal XRD patterns of $1T$ and $2H$-TaS_2 and the corresponding pictures. (b) The powder XRD pattern of the crushed $4H_b$-TaS_2 crystals measured at room temperature. (c) The temperature dependence of in-plane resistivity (ρ_{ab}) of $4H_b$-TaS_2, inset presents the enlargement of superconducting transition at the low temperature region. (d) ZFC and FC magnetic susceptibility of $4H_b$-TaS_2 measured at $H = 10$ Oe, perpendicular to the *ab* plane. The inset shows the magnetic hysteresis loop at $T = 2$ K.

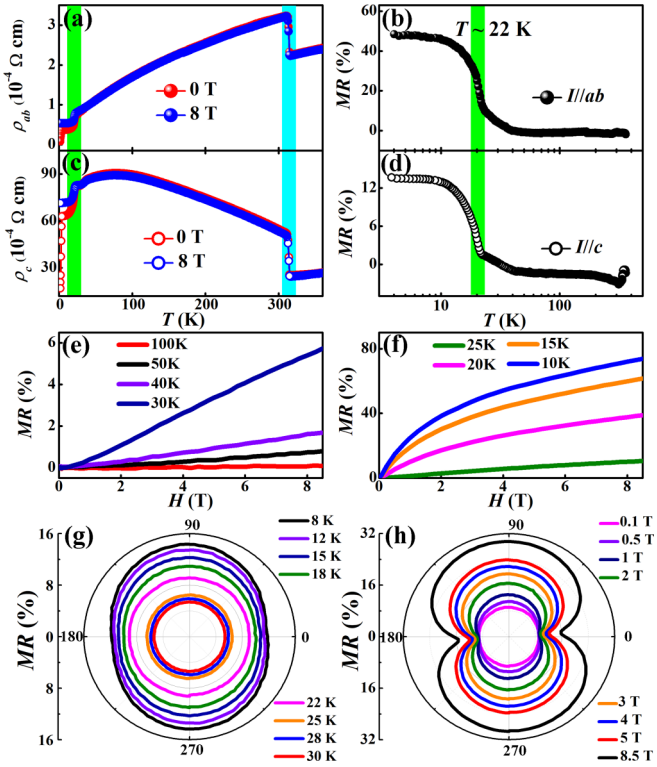

FIG. 3. The temperature dependence of (a) ρ_{ab} /(c) ρ_c at 0 T and 8 T, and the corresponding MR is displayed in (b)/(d). (e), (f) The field dependence of MR at different temperatures. (g) The angular dependent MR data under $H = 0.1$ T at different temperatures around 22 K. (h) AMR with various magnetic fields at 22 K.

inset of Fig. 2(c). However, the transition would become sharp when external pressure is applied [32]. Figure 2(d) shows the temperature-dependent magnetization in the zero-field and field cooling (ZFC and FC) modes with the magnetic field of 10 Oe. The T_c defined by the onset point is about 3.3 K, which is consistent with the resistivity result. The hysteresis loop at 2 K [see the inset of Fig. 2(d)] suggests a typical type-II superconducting behavior of $4H_b$-TaS_2.

We also measured the in-plane resistivity ρ_{ab} and inter-plane resistivity ρ_c at 0 T and 8 T, respectively. The resistivity curves exhibit large anisotropy (see Fig. S2 for ρ_{ab}/ρ_c in the supporting materials [33]): For ρ_{ab}, the current mainly flows through the metallic trigonally coordinated layers, while the current must pass through the semimetallic octahedrally coordinated layers for ρ_c, and this higher resistivity dominates that of the intervening metallic layers below 315 K. However, when the magnetic field of 8 T is applied, ρ_{ab} and ρ_c both increase significantly, especially below 22 K, which indicates the emergence of positive MR. We plotted the MR as a function of temperature with different current directions in Figs. 3(b) and 3(d). It shows that the value of MR is negligible in the part of high temperature, which is close to 0 (only a quite small kink occurs near 315 K). When the temperature drops and approaches 22 K, MR rises rapidly, and as the temperature continues to decrease, it continuously increases. Considering the temperature of 22 K, at which the *H* layers happen to form the 3×3 CDW structures, it suggests that the increase in MR is closely related to the formation of CDW. The field dependence of MR at different temperatures is also presented in Figs. 3(e) and 3(f). We find that MR increases linearly with the magnetic field above 22 K, but when the temperature decreases to the low CDW transition, MR increases significantly, and the curves gradually deviate from the linearity. Although the value of MR below 22 K in $4H_b$-TaS_2 cannot be compared with other MX_2 materials with extremely large MR, such as $MoTe_2$ [37], the relatively large MR is rare in polymorphs of TaS_2. It also reflects the potential of heterostructure $4H_b$-TaS_2 in practical applications. In addition, we have investigated the relationship between the angular and MR with $I//ab$ (the measurement configuration of the AMR can be found in Fig. S4 in the Supplemental Material [33]). When a small field of 0.1 T was applied, we found that MR changed from isotropy to twofold symmetry with the temperature decreases, and the critical temperature was 22 K, as seen in Fig. 3(g). Here we can understand the phenomenon simply: The current mainly flows through the metallic *H* layers when the temperature is higher than 22 K, and no special electronic structures are formed on the *H* layers, which can be regarded as isotropic. As the temperature drops below 22 K, the 3×3 CDW structures would be found in *H* layers. At this point, the different CDW structures of

H and T layers both contribute to the symmetry. Therefore, the appearance of the twofold symmetry can be considered as the result of superimposed effect. To further study the effect of the magnetic field on this symmetry transition, AMR under different fields at 22 K is indicated in Fig. 3(h). When the field is increased to 0.5 T, the twofold symmetry has emerged. The gourd-shaped MR can be observed for each magnetic field (from 0.5 to 8.5 T) and becomes enhanced with increasing fields. Considering charge transfer between T and H layers, the magnetic field may play a role in suppressing it, which is consistent with the occurrence of positive MR. It is worth noting that the shape of AMR shown here is different from the twofold-symmetrical MR in other materials reported previously [38,39], mainly due to the values of 0° and 180° in $4H_b$-TaS_2 not being close to zero. The appearance of this shape may be the result of some superimposed effects and requires further experimental verification.

Generally, several mechanisms were proposed to explain the origin of MR in materials without magnetic ions: (i) the strong spin-orbit coupling (SOC) should be considered in some materials like WTe_2 [40], (ii) the linear dispersion of band in the momentum space would cause the larger MR in some Dirac semimetals [41,42], (iii) the electron-hole (e-h) compensation has also played a major role in the generation of MR [43–45]. For $4H_b$-TaS_2, its band structure is almost unchanged with considering SOC according to the calculation results (see the supporting materials for the band structure with SOC [33]). Besides, we have not observed any significant linear dispersion from the band structure in Fig. 1(f). Therefore, the possibilities of the first two origins can be ruled out. To determine whether the larger MR is originated from the e-h compensation or related to the factors such as carrier density and so on, we have also carried out the Hall effect measurements on the $4H_b$-TaS_2 single crystal. Figures 4(a) and 4(b) display ρ_{yx} as a function of the magnetic field for a fixed temperature ranging from 10 K to 320 K. The temperature-dependent Hall coefficient (R_H) is presented in Fig. 4(c). Above 22 K, as the temperature decreases, R_H is positive and increases slowly, indicating that the dominant carrier is hole-type. While below 22 K, R_H decreases rapidly with the temperature decreasing and becomes negative, which means the electron-type carriers gradually dominate. The specific carrier density and mobility can also be obtained by fitting the Hall conductivity σ_{xy} ($\sigma_{xy} = \rho_{yx}/(\rho_{xy}^2 + \rho_{xx}^2)$). First, we try to fit σ_{xy} by semiclassical two-band model and obtain the evolution of temperature-dependent carrier concentrations and mobilities (see Part IV in the Supplemental Material for details [33]). Based on the two-band model, we find that the holes dominate at the high-temperature state, when the temperature drops below 22 K, the concentration of electrons rises rapidly. Although the hole concentration reduces with decreasing temperature, the mobility of holes rises sharply. According to the four parameters of carriers obtained by the two-band model, we can also obtain the theoretical temperature-dependent MR under the magnetic field of 8 T, as shown in Fig. 4(e) (the derivation process can be found in Part V of the Supplemental Material [33]). By comparing Fig. 4(d) and Fig. 4(e), it is clear that although both of the curves rise sharply around 22 K, the calculated MR begins to reduce with decreasing temperature after reaching the peak at about

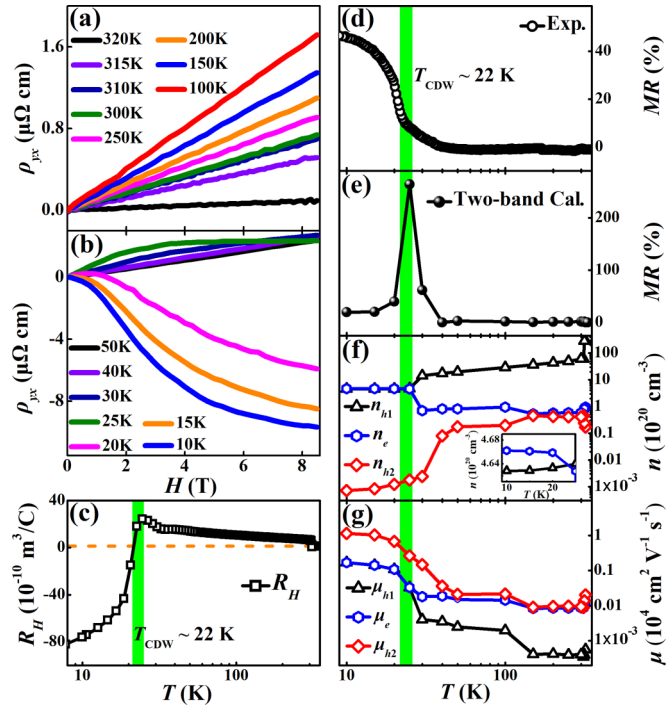

FIG. 4. The field dependence of Hall resistivity $\rho_{yx}(H)$ at (a) 320–100 K and (b) 50–10 K, respectively. (c) The temperature-dependent Hall coefficient R_H. The temperature dependence of (d) measured MR and (e) calculated MR based on the two-band model. The temperature-dependent (f) density of electrons/holes n_e/n_h, and (g) carrier mobility μ_e/μ_h (extracted from the multiband fitting of σ_{xy} in Fig. S6).

T_{CDW}, which is obviously different from the experimental result. It suggests that the two-band model cannot describe the transport properties of $4H_b$-TaS_2 successfully, especially below $T_{CDW} \sim 22$ K, as it consists of more than two bands due to the complexity of the Fermi surface. The two-band model may be too simple to describe the Hall conductivity, therefore, we try to use the multiband model [45] to explore the detailed information of the carriers in $4H_b$-TaS_2. The multiband model can well fit the σ_{xy} below and above $T_{CDW} \sim 22$ K (see Fig. S6 in the Supplemental Material [33]), and we obtain two types of holes (h_1 and h_2) and one type of electrons through the fitting. The information of carriers is displayed in Figs. 4(f) and 4(g). We can observe that the h_1 with low mobility in the high-temperature state dominates, which remains to the vicinity of the transition temperature. However, the concentration of h_1 gradually reduces with the decreasing temperature, especially around 22 K, the reduction is quite obvious. Meanwhile, the electron concentration increases sharply around 22 K, and the two gradually approach the state of compensation. While the concentration of h_2 is low, its mobility rises rapidly with the decreasing temperature and reaches a relatively high value $\sim 1.15 \times 10^4$ cm^2 V^{-1} s^{-1} at 10 K, which is consistent with the characteristic that MR continues to rise without reaching saturation below 22 K. Similarly, the huge contribution of high mobility to MR can also be found in some materials, such as Cd_3As_2, $NbSb_2$, and so on [46,47]. The results of multiband fitting may reflect that the large MR in $4H_b$-TaS_2

stems from partial compensation (h_1 from high-temperature state and electrons from low-temperature state) and high mobility of h_2. Commonly, the origin of MR in many materials cannot be attributed to one certain effect. Besides the partial compensation effect, the high mobility of h_2 in $4H_b$-TaS_2 also cannot be ignored. The unified understanding of the origin of MR in $4H_b$-TaS_2 needs further research.

IV. CONCLUSION

In conclusion, we have comparatively investigated the features of the band structure, Fermi surface, and the structures of $1T$, $2H$, and $4H_b$-TaS_2 through the first-principles calculations and basic physical measurements. The results of systematic electrical transport measurements carried on $4H_b$-TaS_2 suggest the occurrence of MR at low temperature, which stems from partial compensation and high mobility of one hole band. In addition, the symmetry of MR under the low magnetic field has also changed significantly in $4H_b$-TaS_2 based on the results of AMR, which is closely related to the CDW structures formed in the H layers at 22 K. The presence of MR in $4H_b$-TaS_2 suggests the potential applications for functional devices in the future.

ACKNOWLEDGMENTS

The authors thank Prof. Shichao Yan from Shanghai Tech University for fruitful discussions and Dr. Archana Tiwari from University of Waterloo for her assistance in editing the revised paper. This work was supported by the National Key Research and Development Program under Contract No. 2016YFA0300404 and the National Nature Science Foundation of China under Contracts No. 11674326, No. 11874357, No. 11774351, No. 11974061, the Joint Funds of the National Natural Science Foundation of China and the Chinese Academy of Sciences' Large-Scale Scientific Facility under Contracts No. U1832141, No. U1932217 and the Key Research Program of Frontier Sciences, CAS (QYZDB-SSW-SLH015) and The Users with Excellence and Scientific Research Grant of Hefei Science Center of CAS (2018HSC-UE011), and the Open Project of State Key Laboratory of Superhard Materials, Jilin University (No. 201902).

J.J.G. and J.G.S. have contributed equally to this work.

[1] A. S. Ngankeu, S. K. Mahatha, K. Guilloy, M. Bianchi, C. E. Sanders, K. Hanff, K. Rossnagel, J. A. Miwa, C. Breth Nielsen, M. Bremholm, and P. Hofmann, Phys. Rev. B **96**, 195147 (2017).

[2] J. Zhou, J. Lin, X. Huang, Y. Zhou, Y. Chen, J. Xia, H. Wang, Y. Xie, H. Yu, J. Lei, D. Wu, F. Liu, Q. Fu, Q. Zeng, C. H. Hsu, C. Yang, L. Lu, T. Yu, Z. Shen, H. Lin *et al.*, Nature (London) **556**, 355 (2018).

[3] R. Salgado, A. Mohammadzadeh, F. Kargar, A. Geremew, C. Y. Huang, M. A. Bloodgood, S. Rumyantsev, T. T. Salguero, and A. A. Balandin, Appl. Phys. Express **12**, 037001 (2019).

[4] X. Y. Zhu, S. Wang, Z. Y. Jia, L. Zhu, Q. Y. Li, W. M. Zhao, C. L. Xue, Y. J. Xu, Z. Ma, J. Wen, S. L. Yu, J. X. Li, and S. C. Li, Phys. Rev. Lett. **123**, 206405 (2019).

[5] B. S. Wang, Y. Liu, X. Luo, K. Ishigaki, K. Matsubayashi, W. J. Lu, Y. P. Sun, J. G. Cheng, and Y. Uwatoko, Phys. Rev. B **97**, 220504(R) (2018).

[6] W. Fu, Y. Chen, J. H. Lin, X. W. Wang, Q. S. Zeng, J. D. Zhou, L. Zheng, H. Wang, Y. M. He, H. Y. He, Q. D. Fu, K. Suenaga, T. Yu, and Z. Liu, Chem. Mater. **28**, 7613 (2016).

[7] M. Klanjšek, A. Zorko, R. Žitko, J. Mravlje, Z. Jagličić, P. K. Biswas, P. Prelovšek, D. Mihailovic, and D. Arčon, Nat. Phys. **13**, 1130 (2017).

[8] M. Kratochvilova, A. D. Hillier, A. R. Wildes, L. Wang, S. W. Cheong, and J. G. Park, npj Quantum Mater. **2**, 42 (2017).

[9] A. Ribak, I. Silber, C. Baines, K. Chashka, Z. Salman, Y. Dagan, and A. Kanigel, Phys. Rev. B **96**, 195131 (2017).

[10] Y. J. Yu, Y. Xu, L. P. He, M. Kratochvilova, Y. Y. Huang, J. M. Ni, L. Wang, S. W. Cheong, J. G. Park, and S. Y. Li, Phys. Rev. B **96**, 081111(R) (2017).

[11] J. Joshi, H. M. Hill, S. Chowdhury, C. D. Malliakas, F. Tavazza, U. Chatterjee, A. R. Hight Walker, and P. M. Vora, Phys. Rev. B **99**, 245144 (2019).

[12] D. C. Freitas, P. Rodière, M. R. Osorio, E. Navarro-Moratalla, N. M. Nemes, V. G. Tissen, L. Cario, E. Coronado, M. García-Hernández, S. Vieira, M. Núñez-Regueiro, and H. Suderow, Phys. Rev. B **93**, 184512 (2016).

[13] R. Grasset, Y. Gallais, A. Sacuto, M. Cazayous, S. Manas-Valero, E. Coronado, and M. A. Measson, Phys. Rev. Lett. **122**, 127001 (2019).

[14] J. G. Checkelsky, M. Lee, E. Morosan, R. J. Cava, and N. P. Ong, Phys. Rev. B **77**, 014433 (2008).

[15] R. R. Cai, W. Y. Xing, H. B. Zhou, B. N. Li, Y. Y. Chen, Y. Y. Yao, Y. Ma, X. C. Xie, S. Jia, and W. Han, Phys. Rev. B **100**, 054430 (2019).

[16] H. W. Zhang, W. S. Wei, G. L. Zheng, J. W. Lu, M. Wu, X. D. Zhu, J. Tang, W. Ning, Y. Y. Han, L. S. Ling, J. Y. Yang, W. S. Gao, Y. L. Qin, and M. L. Tian, Appl. Phys. Lett. **113**, 072402 (2018).

[17] F. J. Di Salvo, B. G. Bagley, J. M. Voorhoeve, and J. V. Waszczak, J. Phys. Chem. Solids **34**, 1357 (1973).

[18] W. J. Wattamaniuk, J. P. Tidman, and R. F. Frindt, Phys. Rev. Lett. **35**, 62 (1975).

[19] H. P. Hughes and J. A. Scarfe, Phys. Rev. Lett. **74**, 3069 (1995).

[20] J. J. Kim and H. Olin, Phys. Rev. B **52**, R14388(R) (1995).

[21] I. Ekvall, J. J. Kim, and H̊. Olin, Phys. Rev. B **55**, 6758 (1997).

[22] A. Ribak, R. Majlin Skiff, M. Mograbi, P. K. Rout, M. H. Fischer, J. Ruhman, K. Chashka, Y. Dagan, and A. Kanigel, Sci. Adv. **6**, eaax9480 (2020).

[23] R. M. Fleming and R. V. Coleman, Phys. Rev. Lett. **36**, 1555 (1976).

[24] R. M. Fleming and R. V. Coleman, Phys. Rev. B **16**, 302 (1977).

[25] G. Kresse and J. Hafner, Phys. Rev. B **48**, 13115 (1993).

[26] G. Kresse and J. Furthmüller, Comput. Mater. Sci. **6**, 15 (1996).

[27] P. E. Blochl, Phys. Rev. B **50**, 17953 (1994).

[28] J. P. Perdew, K. Burke, and M. Ernzerhof, Phys. Rev. Lett. **77**, 3865 (1996).
[29] A. Kokalj, Comput. Mater. Sci. **28**, 155 (2003).
[30] N. J. Doran, G. Wexler, and A. M. Woolley, J. Phys. C: Solid State Phys. **11**, 2967 (1978).
[31] J. A. Wilson, F. J. Di Salvo, and S. Mahajan, Adv. Phys. **24**, 117 (1975).
[32] R. H. Friend, R. F. Frindt, A. J. Grant, A. D. Yoffe, and D. Jerome, J. Phys. C: Solid State Phys. **10**, 1013 (1977).
[33] See Supplemental Material at http://link.aps.org/supplemental/10.1103/PhysRevB.102.075138 for details on the electrical transport measurements, band structure with SOC, measurement schematic diagram of AMR, calculation process of MR, and the two-band/multiband model fitting, which includes Refs. [34–36].
[34] C. M. Hurd, *The Hall Effect in Metals and Alloys* (Cambridge University, Cambridge, England, 1972).
[35] M. N. Ali, J. Xiong, S. Flynn, J. Tao, Q. D. Gibson, L. M. Schoop, T. Liang, N. Haldolaarachchige, M. Hirschberger, N. P. Ong, and R. J. Cava, Nature (London) **514**, 205 (2014).
[36] Y. Luo, H. Li, Y. M. Dai, H. Miao, Y. G. Shi, H. Ding, A. J. Taylor, D. A. Yarotski, R. P. Prasankumar, and J. D. Thompson, Appl. Phys. Lett. **107**, 182411 (2015).
[37] F. C. Chen, H. Y. Lv, X. Luo, W. J. Lu, Q. L. Pei, G. T. Lin, Y. Y. Han, X. B. Zhu, W. H. Song, and Y. P. Sun, Phys. Rev. B **94**, 235154 (2016).
[38] N. J. Ghimire, M. A. Khan, A. S. Botana, J. S. Jiang, and J. F. Mitchell, Phys. Rev. Materials **2**, 081201(R) (2018).
[39] X. Luo, R. C. Xiao, F. C. Chen, J. Yan, Q. L. Pei, Y. Sun, W. J. Lu, P. Tong, Z. G. Sheng, X. B. Zhu, W. H. Song, and Y. P. Sun, Phys. Rev. B **97**, 205132 (2018).
[40] J. Jiang, F. Tang, X. C. Pan, H. M. Liu, X. H. Niu, Y. X. Wang, D. F. Xu, H. F. Yang, B. P. Xie, F. Q. Song, P. Dudin, T. K. Kim, M. Hoesch, P. K. Das, I. Vobornik, X. G. Wan, and D. L. Feng, Phys. Rev. Lett. **115**, 166601 (2015).
[41] T. Liang, Q. Gibson, M. N. Ali, M. Liu, R. J. Cava, and N. P. Ong, Nat. Mater. **14**, 280 (2015).
[42] J. Xiong, S. K. Kushwaha, T. Liang, J. W. Krizan, M. Hirschberger, W. Wang, R. J. Cava, and N. P. Ong, Science **350**, 413 (2015).
[43] L. K. Zeng, R. Lou, D. S. Wu, Q. N. Xu, P. J. Guo, L. Y. Kong, Y. G. Zhong, J. Z. Ma, B. B. Fu, P. Richard, P. Wang, G. T. Liu, L. Lu, Y. B. Huang, C. Fang, S. S. Sun, Q. Wang, L. Wang, Y. G. Shi, H. M. Weng *et al.*, Phys. Rev. Lett. **117**, 127204 (2016).
[44] S. S. Sun, Q. Wang, P. J. Guo, K. Liu, and H. C. Lei, New J. Phys. **18**, 082002 (2016).
[45] J. Xu, N. J. Ghimire, J. S. Jiang, Z. L. Xiao, A. S. Botana, Y. L. Wang, Y. Hao, J. E. Pearson, and W. K. Kwok, Phys. Rev. B **96**, 075159 (2017).
[46] A. Narayanan, M. D. Watson, S. F. Blake, N. Bruyant, L. Drigo, Y. L. Chen, D. Prabhakaran, B. Yan, C. Felser, T. Kong, P. C. Canfield, and A. I. Coldea, Phys. Rev. Lett. **114**, 117201 (2015).
[47] K. Wang, D. Graf, L. Li, L. Wang, and C. Petrovic, Sci. Rep. **4**, 7328 (2014).